J Mater Sci (2022) 57:8425–8441

Advanced Nanomaterials

Dynamic mechanical behavior and microstructural evolution of additively manufactured 316L stainless steel

Hongyu Yu[1], Rong Chen[2], Wenyang Liu[1,3,*], Simeng Li[1,3], Ling Chen[1], and Shujuan Hou[1]

[1] *State Key Laboratory of Advanced Design and Manufacturing for Vehicle Body, Hunan University, Changsha 410082, China*
[2] *National University of Defense Technology, College of Liberal Art and Sciences, Changsha 410008, China*
[3] *Hunan Provincial Key Laboratory of Intelligent Laser Manufacturing, Hunan University, Changsha 410082, China*

Received: 18 September 2021
Accepted: 28 November 2021
Published online: 3 January 2022

ABSTRACT

The high strain rate dynamic behavior of additively manufactured (AM) 316L stainless steel (SS) is investigated, and a dynamic deformation-induced microstructural evolution is examined in this study. First, the as-built microstructure feature is characterized. The grain morphology is revealed to be location-dependent and driven by the solidification process. A steep rise in the point-to-origin misorientation profile traversing a melt pool boundary is observed, quantitatively describing the influence of process-induced interface on the initial grain orientation state. The static and dynamic mechanical properties are then examined. Compared with conventional wrought 316L SS, AM 316L SS demonstrates an enhanced mechanical strength under quasi-static compression (with a $\sim$95% increase in yield strength). Under dynamic shearing, strain rate-induced strength enhancement is observed in wrought 316L SS (with a $\sim$47% increase in dynamic flow stress); AM 316L SS nevertheless demonstrates nearly rate-insensitive responses in its yield stress (with a $\sim$5% increase in dynamic flow stress). Localized deformation in the form of an adiabatic shear band and the associated structural evolution are analyzed. Radical changes in crystallographic and structural features induced by high strain rate deformation are observed. Grain deformation and rotation lead to a remarkable difference in the grain orientation and spatial direction from the starting state driven by the solidification process. Upon dynamic shearing, the transmission of localized plastic deformation across melt pools is revealed, and the indication in grain rotations is discussed. The change in the geometrically necessary dislocation density is examined, hinting at the competition of the dislocation multiplication and annihilation under localized deformation. The current work

Handling Editor: Sophie Primig.

Address correspondence to E-mail: liuwenyang@hnu.edu.cn

https://doi.org/10.1007/s10853-021-06765-6

enriches the understanding of the dynamic mechanical properties of AM materials at high strain rates.

Introduction

Additive manufacturing is a bottom-up manufacturing technology that produces three-dimensional objects via layer-by-layer stacking of materials [1–3]. As a digital manufacturing method, additive manufacturing can produce difficult-to-manufacture parts with complex structures and shapes, reduce material waste, and integrate multiple components into one [4]. Additive manufacturing technologies for producing metallic parts include selective laser melting (SLM) [5, 6], selective electron beam melting (SEBM) [7, 8], and direct energy deposition (DED) [9, 10]. Despite great application prospects in aeronautical, aerospace, and mechanical industries, critical issues, such as anisotropy and heterogeneity, must be addressed [11–13].

Highly variable material properties are closely associated with unique physical processes involved in additive manufacturing. As a thermal process, laser-based additive manufacturing involves rapid melting and rapid solidification, which lead to the inherent complexity of the as-deposited microstructures [14]. High-temperature gradients and dynamic melt flow are present in melt pools driven by a moving energy source [15]. As a consequence, complex grain morphology and crystallographic texture in as-built materials arise from manufacturing processes [16]. Furthermore, repeated thermal cycles due to the deposition of newly melted layers lead to the evolution of internal unbalanced microstructures [17, 18]. Thus, AM materials often demonstrate an anisotropic mechanical response with large variations in strength and ductility [15]. Rapid solidification also results in a high as-built dislocation density, imposing an important effect on mechanical properties [19]. Unique microstructural characteristics are key to the process-property linkage in AM materials.

While appreciable progress toward understanding the mechanical properties of AM metals has been made in recent years [20], knowledge of the dynamic mechanical behavior of AM materials is still insufficient. Under high rates of deformation, the rate effect is intertwined with the underlying microstructure [21–23], altering the kinematics and kinetics of viscoplastic flow [24]. Thus, dynamic responses differ evidently from those occurring under static or quasi-static conditions. At higher strain rates, various forms of dynamic failure occur, such as an adiabatic shear band (ASB) [25–28], severe plastic deformation (SPD) [20], and failure mode transition (FMT) [22]. Recent progress includes anisotropy in the impact toughness [5], spallation responses [29, 30], dynamic mechanical properties [31, 32], and the influence of porosity [33]. The complex microstructural characteristics of AM metals tend to impact the dynamic mechanical properties.

The objective of this study is mainly to investigate the dynamic deformation of 316L SS manufactured by the DED process under high strain rates, particularly, the microstructural evolution upon adiabatic shear localization. We conducted high strain rate dynamic shear tests (strain rate >2000 s^{-1}) and quasi-static compression tests. The yield strength of the quasi-statically compressed AM 316L SS demonstrates a greatly enhanced yield strength compared with that of wrought 316L SS. Interestingly, nearly rate-insensitive responses in the yield stress are noticed for AM 316L SS under dynamic loading. Microstructural characterization reveals that the occurrence of adiabatic shear localization is accompanied by a severe change of grain morphologies. Microstructural evolution including grain rotation and refinement is analyzed, and its relationship with material hardening and failure is discussed.

In the following sections, the preparation and classification of test specimens are presented, followed by the analysis of the initial microstructure. Then, starting from the quasi-static experiment and the dynamic impact experiment, the mechanical properties are analyzed. Next, the relationship between the high as-built dislocation density and the yield strength of the material is discussed, and various failure mode processes and their underlying microstructure evolutions are explored. Finally, the characterization of the grain rotations and crystallographic textures in the plastic deformation failure process is established via the grain orientation density contour maps.

Material and experimental techniques

Material and specimens

This study involves production, microstructural characterization, quasi-static compression, and dynamic shear testing of 316L stainless steel manufactured by DED–a type of additive manufacturing process that uses a nozzle to blow powder into laser-heated melt pools [10]. The system is equipped with a YLS4000CL fiber laser. An argon atmosphere is used to prevent oxidation during DED processing. The particle size of the commercially available powder is approximately 125μm produced by gas atomization. The nominal chemical composition of the powder from the manufacturer is listed in Table 1.

The bulk blocks of AM 316L SS are built on a base plate, as shown in Figure 1a. The dimensions of the deposited cuboids are 55 mm $\times$12 mm $\times$12 mm. The back-and-forth laser scanning strategy is employed with fixed processing parameters of laser power (600 W), spot diameter (1.2 mm), hatching spacing (1.0 mm), laser scanning speed (480 mm/min), and layer thickness (0.16 mm). A pulsed-wave laser [34] is used in DED.

The cylindrical specimens for quasi-static compression are electro-discharge machines (EDMs) cut from bulk blocks. The dimensions are 10 mm in height along the build direction and 5 mm in diameter. According to the loading direction in relation to the laser scan direction, $C_{\parallel}$ and $C_{\perp}$ specimens are prepared as shown in Figure 2a. Quasi-static compression tests are carried out in an Instron universal testing machine at a compression speed of 2 mm/min and with MoSi2 lubrication to minimize interface friction.

To examine the effect of process-induced anisotropy on dynamic shear behavior, shear planes perpendicular or parallel to the scan tracks, denoted by $S_{\parallel}$ and $S_{\perp}$, respectively, in Figure 1b, are defined. Flat hat-shaped specimens [35] are used to investigate localized deformation. In accordance with the $S_{\parallel}$ and $S_{\perp}$ shear planes, two flat hat-shaped shear specimens of different orientations, as shown in Figure 2b, are EDM cut from bulk blocks.

Dynamic shear tests

Dynamic shear tests (strain rate >2000 s^{-1}) are performed at room temperature by means of the split-Hopkinson pressure bar (SHPB) technique [36]. The flat hat-shaped specimen used for dynamic shear testing is located between the incident and transmitter bars. The SHPB tests are lubricated with MoSi2 to minimize friction at the sample-pressure bar interfaces. A series of dynamic loading experiments are performed on flat hat-shaped specimens using stopper rings to control the displacements (0.7 and 1.7 mm). The area of the shear region of the flat hat-shaped specimen is expressed as

$$A = \frac{\pi(d_i + d_e)h}{2}, \tag{1}$$

where d_i is the width of the hat, d_e is the width of the base hole, and h is the height of the shear compression region.

The signals are monitored using strain gauges. The incident, reflected, and transmitted strain waves–denoted by ε_i, ε_r, and ε_t, respectively–are used to calculate the forces, displacements, and strains. The shear stress in the shear compression region can be estimated as [32]

$$\tau_s(t) = \frac{2\sqrt{5}E_0A_0\varepsilon_t(t)}{5A}, \tag{2}$$

where A_0 is the cross-sectional area of the bar and E_0 is Young's modulus, respectively. The applied force F_s on the specimen can be determined by

$$F_s(t) = A_0E_0\frac{\varepsilon_i + \varepsilon_r + \varepsilon_t}{2}. \tag{3}$$

The incident and transmitter bars are of the same diameter, yielding the relationship $\varepsilon_t = \varepsilon_i + \varepsilon_r$ [36]. Consequently,

$$F_s(t) = A_0E_0\varepsilon_t(t). \tag{4}$$

When the specimen is in a state of one-dimensional stress waves and uniform stress, the histories of displacement (approximately estimated as the top-to-bottom surface displacement [32]) can be determined by

Table 1 Nominal chemical composition of AM 316L SS powder

composition	C	Cr	Mn	Mo	Nb	Ni	Si	Fe
Wt. %	0.02	16.7	1.80	2.00	0.02	10.00	0.50	bal.

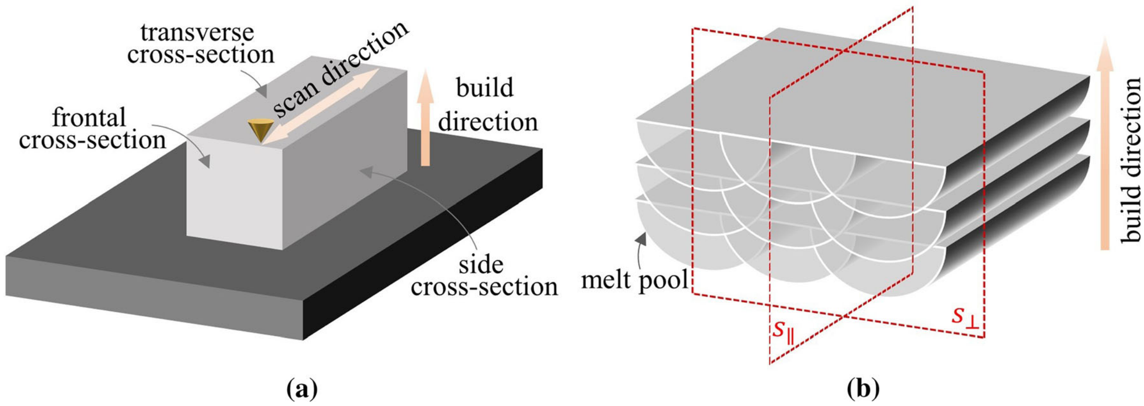

Figure 1 **a** Block of deposited materials for specimen preparation. The transverse cross section is perpendicular to the build direction, and the frontal cross section is perpendicular to the scan direction. **b** Shear planes $S_{\parallel}$ and $S_{\perp}$ defined in relation to melt pools.

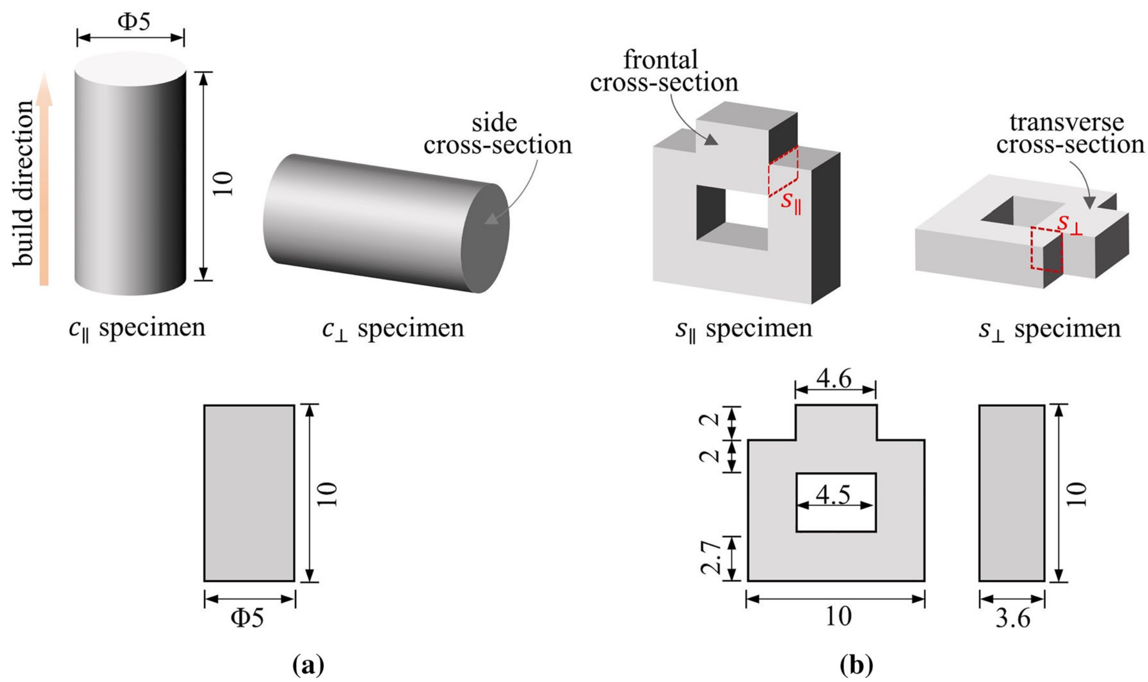

Figure 2 **a** $C_{\parallel}$ and $C_{\perp}$ specimens for quasi-static compression; **b** $S_{\parallel}$ and $S_{\perp}$ specimens that facilitate the occurrence of localized deformation under dynamic compression. All dimensions are given in mm.

$$\Delta u_s(t) = -2C_0 \int_0^t \varepsilon_r(t)dt, \quad (5)$$

where C_0 is the elastic wave speed. The longitudinal strain can be approximated by

$$\varepsilon(t) \approx \frac{\Delta u_s(t)}{h}. \quad (6)$$

The shear strain can be calculated by the expression introduced by [26]

$$\gamma(t) = \sqrt{2e^{2\varepsilon(t)} - 1} - 1. \quad (7)$$

The shear tests are performed on flat hat-shaped specimens with the SHPB at 293*K*. Typical strain gauge signals recorded in the SHPB test for the AM 316L SS test and the signals after initiation to zero for elastic wave analysis are shown in Figure 3.

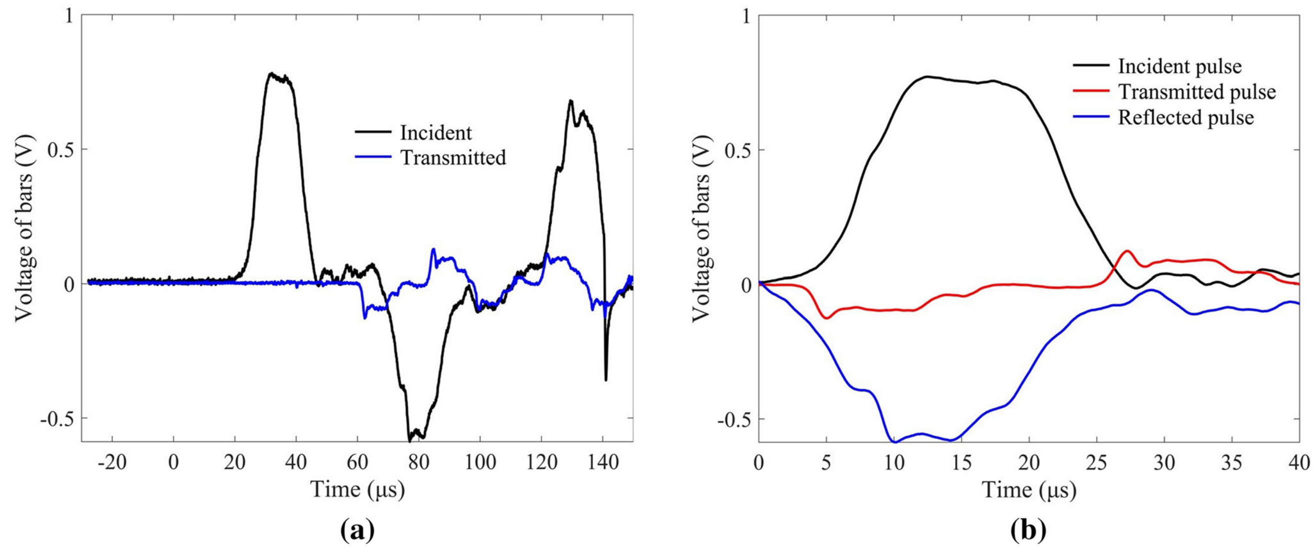

Figure 3 **a** Typical strain gauge signals recorded in the SHPB test at 293*K*; **b** Signals after initiation to zero for elastic wave analysis.

Material characterization

Optical microscopy (OM) and electron backscatter diffraction (EBSD) are used to characterize the microstructures before and after dynamic deformation. Sample preparation for OM consists of grinding on silicon carbide papers with increasingly finer grits, followed by mechanical polishing with alpha-alumina slurry and etching with standard aqua regia prepared by nitric acid and hydrochloric acid. Images at various magnifications are acquired using an Axio Vert. A1 optical microscope. The samples for EBSD analysis are sectioned by electrical discharge machining, and polishing is accomplished using a Leica EM TIC3X argon ion beam polisher. The EBSD analysis is performed with a step size of 0.2μm on a TESCAN MAIA 3 XMH SEM using MTEX Data Analysis software.

Results and discussion

Initial microstructure

The grain structures viewed in the frontal and transverse cross sections (see Figure 2 for definitions) are characterized before the dynamic shear tests. In DED-processed stainless steel, solidification structures with complex morphologies are seen [15]. The size of solidification structures is determined by the thermal gradient and the growth rate, the product of which is high near the melt pool centers and low close to the melt pool boundaries [37].

In the frontal cross section (parallel to the build direction) as shown in Figure 4a with an intersection of melt pool boundaries identified, the major axis of columnar-shaped structures is roughly normal to the melt pool boundaries, as a result of the temperature gradient. The grain morphology is affected by the overlap of deposition tracks as the middle of one melt pool can become the edge of the adjacent melt pool. Note also that melt pool geometry, which can be irregular and deviate from the ideally spaced and aligned configuration, also strongly influences the morphology [38]. In the transverse cross section (perpendicular to the build direction), a majority of grains are nearly equiaxed in shape, as shown in Figure 4b. The three-dimensional characterization [15] has revealed that the roughly equiaxed appearance of grains could be the cross section of columnar grains due to the viewing perspective.

The misorientation profiles along different paths (depicted in Figure 4) are shown in Figure 5. Paths p_1–p_2 and q_1–q_2 are picked such that a melt pool boundary is crossed. Orthogonal paths v_1–v_2 and w_1–w_2 are chosen, given that no apparent process-induced interfaces show up in the transverse cross section. The point-to-point line of misorientation is a measure of the angle between neighboring points that characterizes the correlated distribution; the point-to-origin line of misorientation, appropriate to the

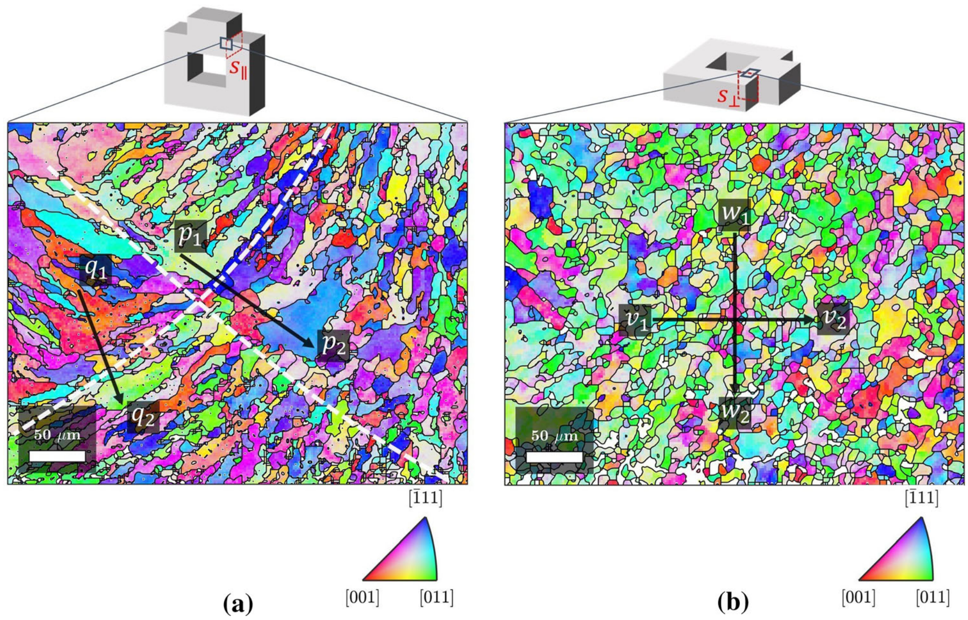

Figure 4 **a** Grain structures viewed in the frontal cross section characterized before dynamic shear tests and (b) grain structures viewed in the transverse cross section characterized before dynamic shear tests. The white dashed lines are the approximate melt pool boundaries.

uncorrelated distribution, is a measure relative to the first point on the path [39].

Figure 5**a** and **b** plots the misorientation profiles along paths p_1–p_2 and q_1–q_2 on the frontal cross section, respectively. Spikes in the point-to-point misorientation profiles are observed when neighboring points are located in different grains across a grain boundary. Interestingly, a steep rise in the point-to-origin misorientation profiles that forms a plateau correlates well with the path traversing melt pool boundaries. A greater difference in grain orientations tends to result in higher resistance to shear slip. In addition, frequent variation in the gradients of the misorientation profiles suggests a higher degree of randomness in grain orientations.

Figure 5c and d plots the misorientation profiles along paths v_1–v_2 and w_1–w_2 on the transverse cross section, respectively. Due to refined grains observed in the transverse cross section, spikes in the misorientation profiles occur at higher frequencies than the frontal cross section. The gradients in the point-to-point or point-to-origin misorientation profile between the two cross sections can be related to the directionality of the deposition tracks. In terms of the heterogeneous microstructure characteristics and combined with the mechanical experimental data, a more in-depth analysis is conducted in the next section.

The stored dislocations depend on processes and material parameters. Different dislocation densities including geometrically necessary dislocations (GNDs), statistically stored dislocations (SSDs), and grain boundary dislocations (GBDs) are interrelated [40]. Misorientations caused by GNDs are measurable by EBSD [41], providing an alternative way for direct observation of GNDs [42]. Theoretical calculations suggest that the GNDs account for the majority of the total dislocation population in DED processed austenitic stainless steel [10]. Figure 6a and b shows the GND density maps from the orientation data presented in Figure 4. A dislocation density of 0.7×10^{14} m^{-2} can be estimated for the frontal cross section and 1.1×10^{14} m^{-2} for the transverse cross section, thereby suggesting a high as-built dislocation density resulting from AM solidification processing. In comparison, annealed wrought 316L SS demonstrates a typical order of $10^9 \sim 10^{10}$ m^{-2} in the dislocation density [20]. The high dislocation density plays a key role in hindering dislocation movements, greatly enhancing the yield strength of AM 316L SS. Figure 6c and d shows the grain reference orientation deviation (GROD) across the entire EBSD maps using the grain mean orientation as the reference. Overall, higher GROD grains are linked with higher GND densities when comparing the GROD and GND maps.

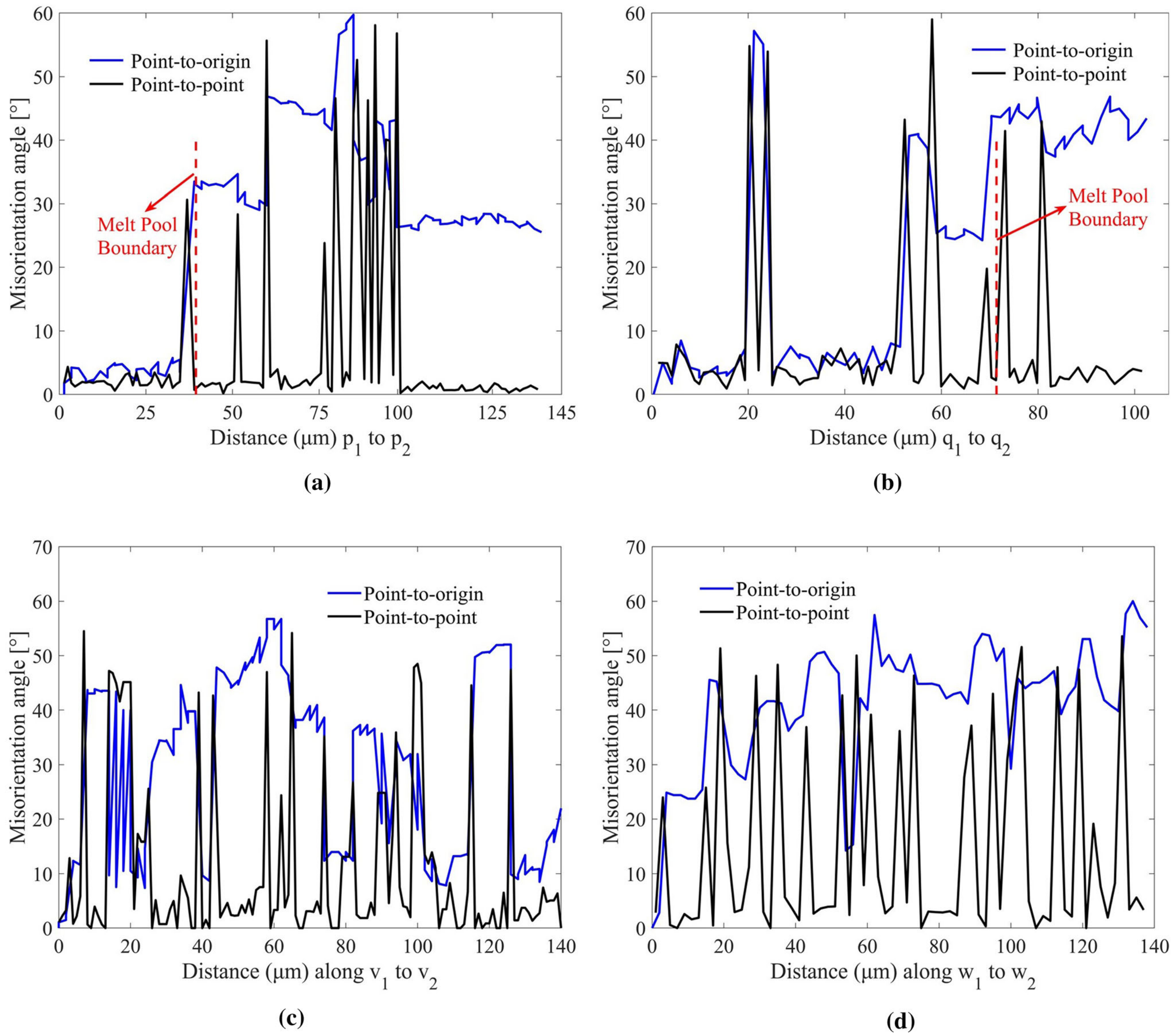

Figure 5 Misorientation profiles along paths (**a**) p_1–p_2 and (**b**) q_1–q_2 of the $S_{\parallel}$ sample; misorientation profiles along paths (**c**) v_1–v_2 and (**d**) w_1–w_2 of the $S_{\perp}$ sample. The drastic variation in the point-to-point or point-to-origin misorientation profile is caused by the traversing of grain boundaries. The red dashed lines correspond to the appearance of melt pool boundaries.

Mechanical properties

Quasi-static compression and strength effect

The comparison of the quasi-static compressive responses for AM and wrought 316L SS is shown in Figure 7a. The as-built AM 316L SS exhibits a remarkably ~95% higher quasi-static compressive yield stress than that of the conventionally manufactured material. After yielding, small but not negligible differences in the rate of work hardening (work-hardening slope) are observed for the AM $C_{\parallel}$ and $C_{\perp}$ specimens. The mechanical anisotropy associated with the build direction (see Figure 1 for orientation reference) has been investigated [43, 44], highlighting the influence of grain morphology and orientation. Wrought manufactured 316L SS, which is considered to be isotropic [29] in the present study, shows a higher slope for work hardening than AM material.

The Hall–Petch relation indicates that the increase in yield strength is proportional to the product of a material-specific constant (K_{HP}) and the inverse square root of the mean grain size [10]

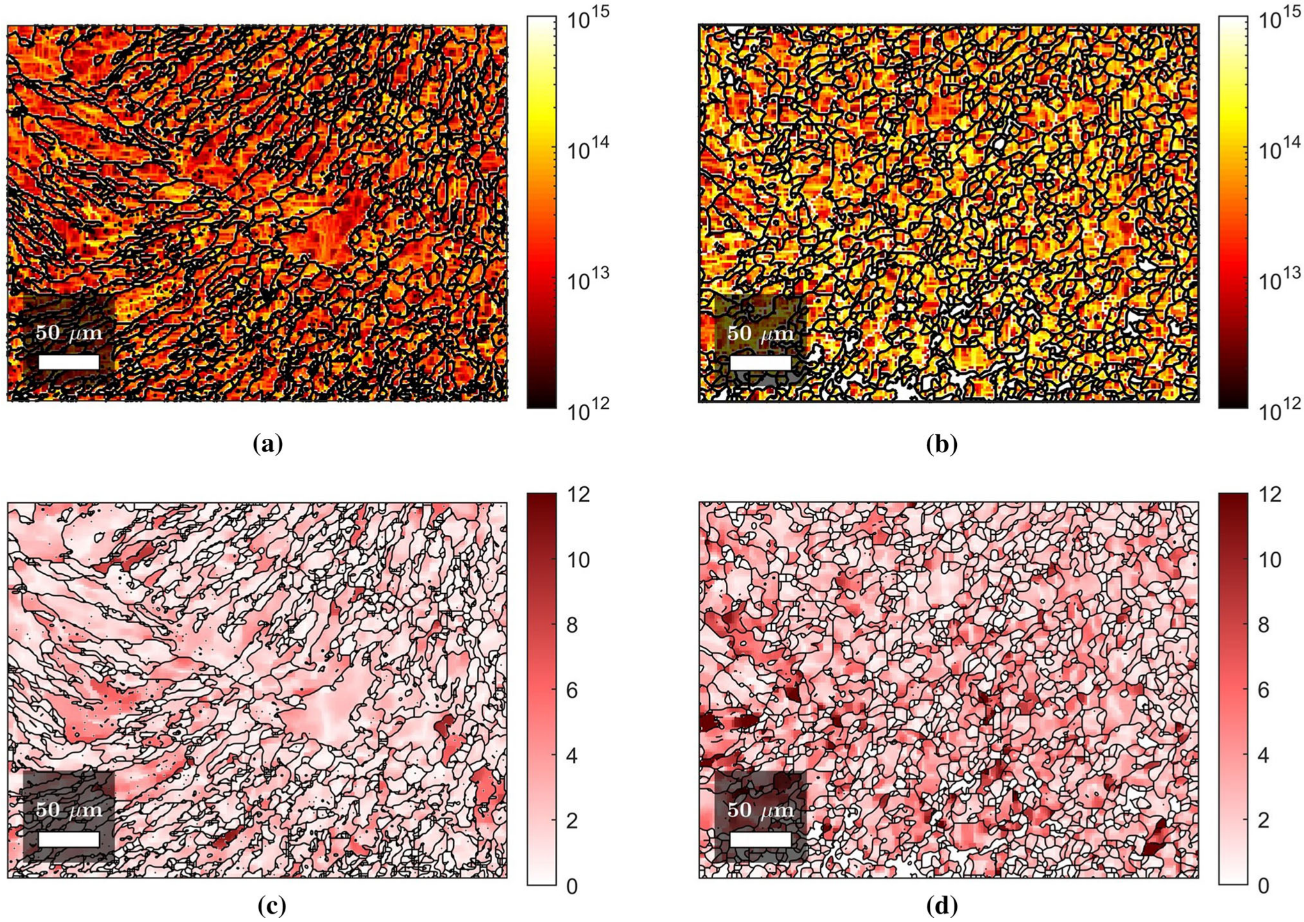

Figure 6 Initial GND density maps of **a** the $S_{\parallel}$ specimen and **b** the $S_{\perp}$ specimen; initial GROD maps of **c** the $S_{\parallel}$ specimen and **d** the $S_{\perp}$ specimen.

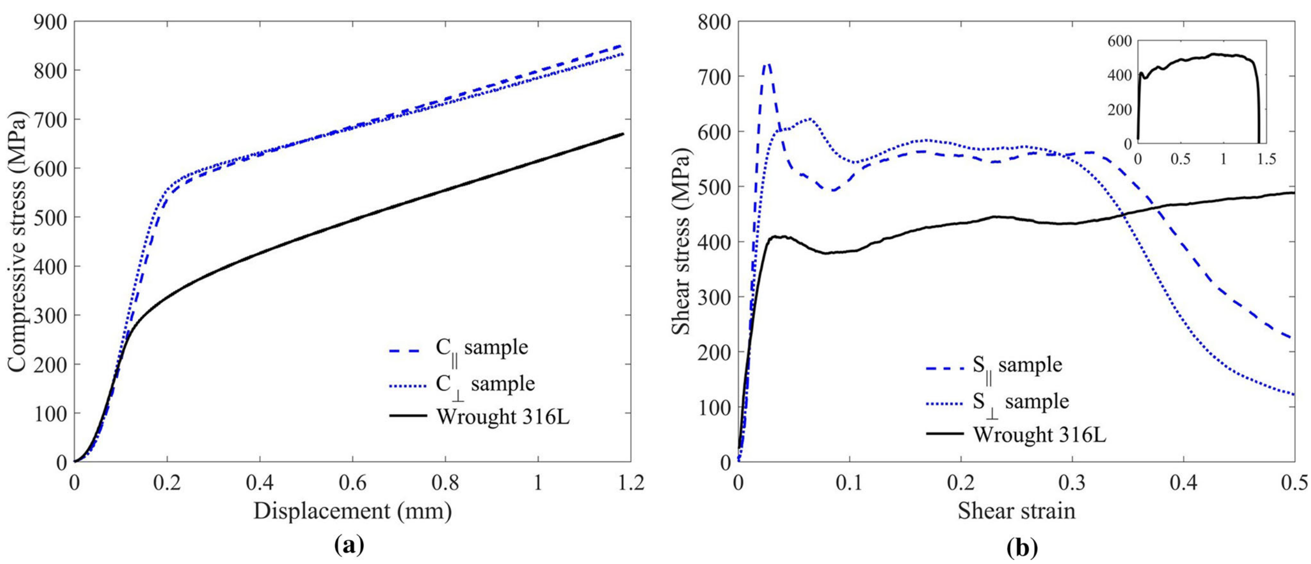

Figure 7 **a** Comparison of the quasi-static compressive response between as-built AM and conventional wrought 316L SS. **b** Comparison of the dynamic shear responses between as-built AM and conventional wrought 316L SS. The figure inset shows the complete stress–strain curve of the wrought sample.

$$\Delta\sigma_y = K_{HP}/\sqrt{D}. \quad (8)$$

Assuming $K_{HP} = 540$ MPa/μm [10], a reduction in the grain size (which is the finest dimension) from $30 \sim 60\mu$m (the grain size of the as-received wrought 316L SS [20]) to $15 \sim 20\mu$m (the grain size of the as-built AM 316L SS extracted from EBSD characterization, see Figure 4) increases the quasi-static yield strength by approximately $22 \sim 70$ MPa. Therefore, the Hall–Petch effect only accounts for part of the increase in the yield strength.

However, the high densities of dislocations (see Figure 6) suggest a significant dislocation strengthening effect in AM 316L SS metals. The Taylor equation indicates that the yield strength varies is proportional to the product of the square root of the dislocation density [45]

$$\Delta\sigma_y = M\alpha Gb\sqrt{\bar{\rho}}. \quad (9)$$

Based on the consideration of the correlation between the yield stress and hardness $\Delta\sigma_y = 3.03\Delta H$ [46] and the correlation between the hardness and dislocation density $\Delta H = C\sqrt{\bar{\rho}}$ (assume $C = 8 \times 10^{-6}$ HV/m [47]), the value of $M\alpha Gb$ is estimated to be 2.424×10^{-5} MPa·m. The estimated dislocation densities of 0.7×10^{14} m/m^3 and 1.1×10^{14} m/m^3 are substituted from the EBSD data presented above. The strengthening effect associated with the GND is 203 and 254 MPa, respectively. We could roughly assume $\bar{\rho} = 1.0 \times 10^{10}$ m^{-2} for the wrought 316L SS, and that the strengthening effect due to contribution of GNDs is about 24 MPa. In comparison, the strengthening effect due to the high as-built GND densities of AM 316L SS is significant, $\Delta\sigma_y = 180 \sim 230$ MPa.

Dynamic compression

Dynamic shear stress–strain curves calculated from the signals of SHPB tests are plotted in Figure 7b. The AM specimens exhibit an abrupt stress–strain transition (jump) from elastic to plastic responses; however, the wrought 316L specimen demonstrates a relatively smooth transition. For the AM $S_{\parallel}$ specimen, the difference between the upper and lower yield stresses is 235 MPa; for the wrought 316L SS, the difference is only 30 MPa.

Upon yielding, the AM $S_{\parallel}$ and $S_{\perp}$ specimens deform in a similarly plastic manner, whereas the wrought specimen demonstrates a gradually increasing strength with increasing strain. The AM specimens fail as the shear strain reaches $\sim 33\%$. The wrought specimen, nevertheless, withstands the same impact loading and can reach $\sim 136\%$ of the shear strain. Therefore, the AM specimens demonstrate a significant reduction in ductility by $\sim 103\%$ under dynamic shear tests.

By comparing quasi-static and dynamic stress–strain curves (see Figure 7a and b), AM 316L SS is found to be less sensitive to the strain rate than wrought 316L SS. The dynamic flow stress of AM 316L SS under dynamic loading is close to the value determined from quasi-static compression (with an increase of $\sim 5\%$), demonstrating nearly strain rate independence. In contrast, the dynamic flow stress of wrought 316L SS evidently increases by approximately $\sim 47\%$ from 278.1 MPa to 409.1 MPa (see Table 2) .

The phenomenon observed in yielding behavior can be related to the as-built dislocation density and the process of solutes diffusing toward dislocations [23]. The mobile solutes tend to cluster near the dislocations and form Cottrell atmospheres [49]. The inherent process characteristics of additive manufacturing lead to high-density solutes [13]. The transient drag force imposed by mobile solutes on moving dislocations reduces the mobile dislocation density as a key influence, thereby inducing upper and lower yield points in the stress–strain curve. The high as-built dislocation density is a likely cause of the insensitivity of AM 316L SS to strain rates.

Dynamic deformation and shear localization

Fracture and the formation of ASB are different failure modes characterized by distinct spatial and temporal scales [21]. The phenomenon of the failure mode transition is closely related to the dynamic loading conditions. When the threshold strain rate is reached, an ASB is initiated as a ductile failure mode. The ASB propagation path is a smooth curve along the maximum shear stress direction, as shown in Figure 8. The time required for the stress wave to propagate through the whole specimen is much shorter than the total duration of the load. After the formation of ASB, the loading does not stop immediately, and the failure of the material still goes on. In this sense, the ASB initiates first, followed by a crack extending along the propagation path of the ASB. The

Table 2 Comparison of the yield stress under quasi-static compression and dynamic shear tests

	AM ∥ specimen	AM ⊥ specimen	wrought specimen
quasi-static yield stress	538.8	549.5	278.1
dynamic flow stress[1]	563.0	583.9	409.1
enhancement	4.5%	6.3%	47.1%

1 shear strain 0.15 [48]

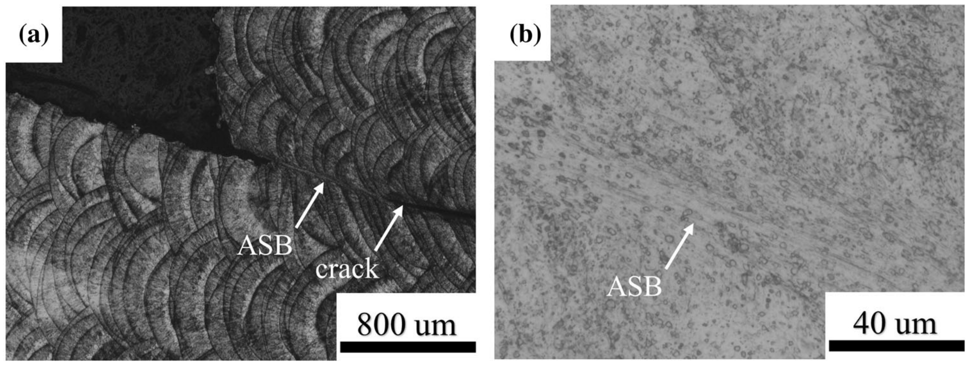

Figure 8 Optical metallurgical micrographs for ASB of AM $S_{\parallel}$ sample **a** 50× and **b** 1000×.

propagation velocity of ASB precedes crack [27], leading to premature failure of the specimen.

The compressive stress applied on the top surface turns into localized shear stress in the flat hat-shaped specimens. Thus, a mode II crack initiates as shown in Figure 9. Below the crack tip (see the gray box of the selected area in Figure 9), the melt pools flow and tend to be blended as a result of SPD. The formation of a thermally softened region might weaken the accumulation of stress and suppress the propagation of crack [50]. The high-density dislocations and refined grains improve the ability to resist deformation [45]. Therefore, the initiated crack only propagates a finite distance without passing through the whole specimen.

Microstructural evolution

Figure 10a is an EBSD map captured near the region of adiabatic shear localization that appeared in the AM $S_{\parallel}$ sample after loading (see Figure 8). The grains are significantly refined in the vicinity of the ASB, and a reduction in size approximately from $\sim 20\ \mu$m to $\sim 2\ \mu$m can be identified. The columnar grains are stretched along the direction of shear deformation due to the emergence of softening effect. Compared with Figure 4a, the phenomenon of columnar grains arranged along the normal directions of the melt pool boundaries no longer appears. The columnar grains near the deformed region tend to rotate to follow the propagation direction of the ASB. The development of adiabatic shear localization can lead to dynamic recrystallization, which is interpreted as an entropic effect arising from the competition between

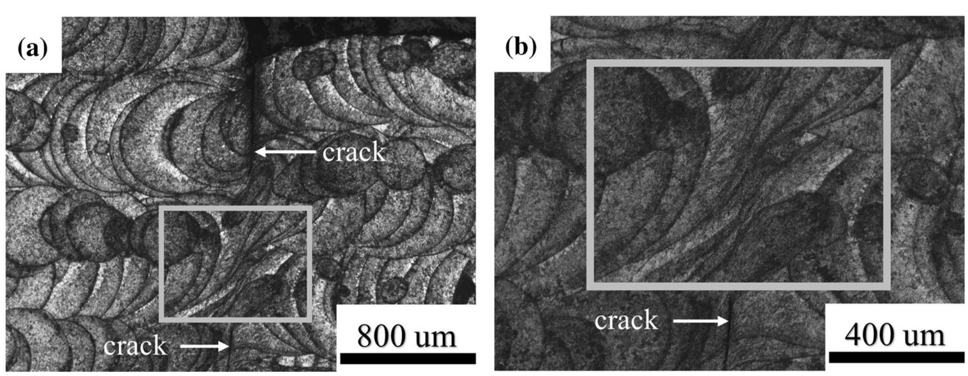

Figure 9 Optical metallurgical micrographs for SPD of AM $S_{\perp}$ sample **a** 50× and **b** 100×.

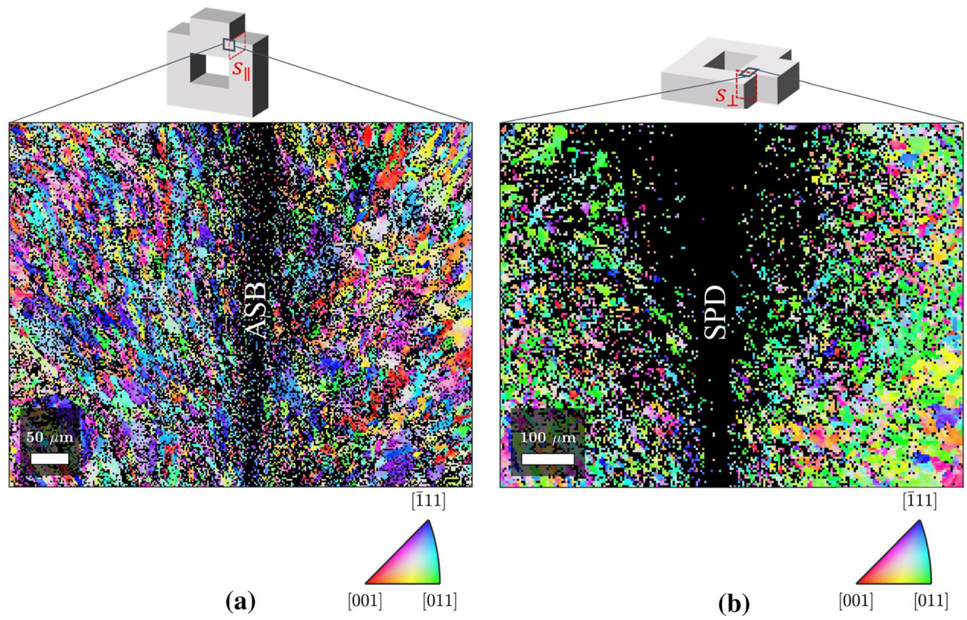

Figure 10 **a** Grain structures viewed in the frontal cross section and **b** grain structures viewed in the transverse cross section characterized after the dynamic shear test.

dislocations generation and grain boundaries re-formation [51].

For the AM $S_{\perp}$ sample after dynamic loading, an EBSD map is generated for the region of interest (the gray box marked in Figure 9) as shown in Figure 10b. The grain size and morphology are evidently different from the initial state (see Figure 4b). Note that the distortions in the crystal lattice result in shifted or degraded EBSD patterns, thereby lowering the quality of diffraction signals in highly deformed regions [52]. The SPD occurs in a localized region along the shear stress transmission path, generating intense dislocation movement and grain refinement. Deformation-induced refinement is affected by multiple factors including dislocation generation, dynamic recrystallization, recovery, and grain boundary migration [53].

For the as-built AM 316L SS, the GND density map demonstrates only a weak change after dynamic loading, as shown in Figure 11. This observation corroborates the small difference in the yield strength of AM 316L SS between the dynamic test and the quasi-static test. The histogram and normalized distribution of GND densities before and after dynamic loading are provided in Appendix A. The shift of peak might be correlated with the competition of the multiplication and annihilation of dislocations [54]. The dislocation generation is enhanced during plastic deformation [55]; the dynamic recrystallization, on the other hand, annihilates dislocations.

Figure 12 plots the inverse pole figure (IPF) of crystallographic orientations obtained for the frontal cross section. After shear deformation, the orientation density is enhanced in all three projection directions. For IPF-x (i.e., the projection plane is perpendicular to the shearing direction), a change in the location of the maximum density is observed. Figure 13 plots the IPF obtained for the transverse cross section, showing that the orientation density is also enhanced after shear deformation. It is noteworthy that the IPF-x of the $S_{\perp}$ and $S_{\parallel}$ specimens demonstrate a similarity in the location of the maximum orientation density after dynamic deformation. Additional pole figures can be found in Appendix B.

The characteristic changes in the dynamic shear stress–strain curves are inseparable from the occurrence of grain rotation during the intense deformation process. In dynamic shear loading, it is considered that the shear stress generates a moment. When a sufficiently large strain occurs in a system, crystals tend to asymptotically rotate toward stable orientations [56]. As a result, the texture strength can be enhanced. In addition, recrystallized grains along the propagation path of ASB can lead to an increase in texture intensities [57].

Figure 11 **a** GND density map of the $S_{\parallel}$ specimen and **b** GND density map of the $S_{\perp}$ specimen after impact deformation.

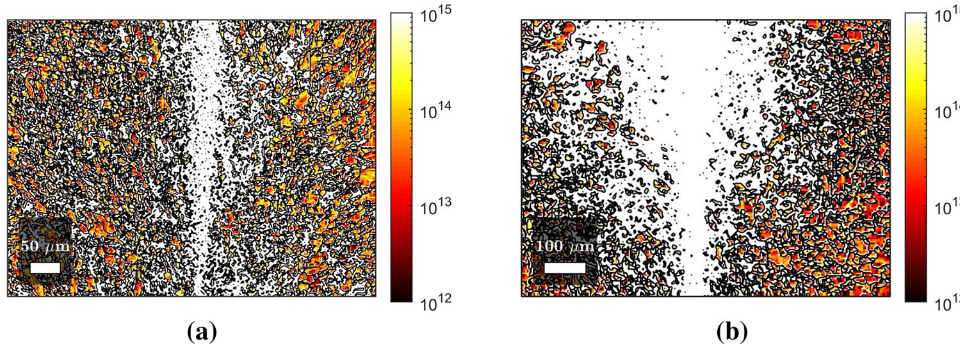

Figure 12 Inverse pole figures of crystallographic orientations obtained for the $S_{\parallel}$ specimen before and after shear deformation.

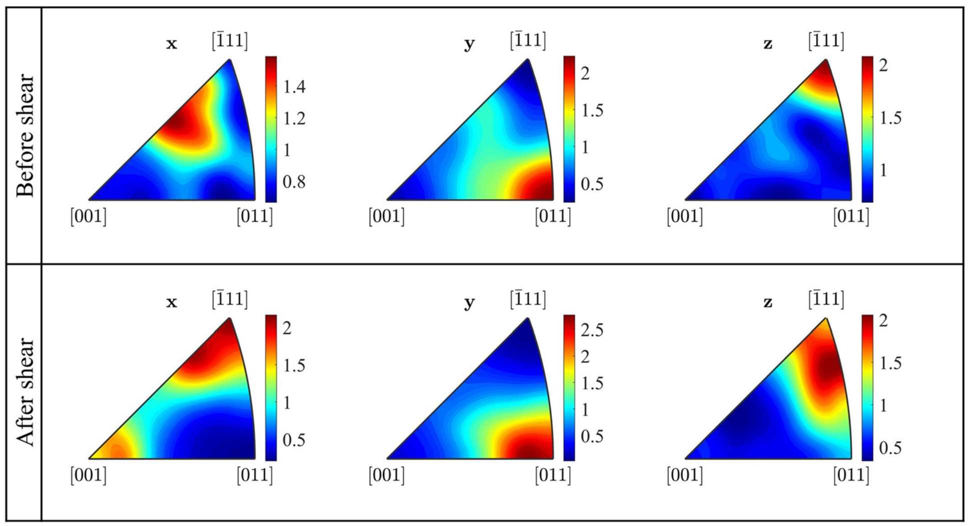

Figure 13 Inverse pole figures of crystallographic orientations obtained for the $S_{\perp}$ specimen before and after shear deformation.

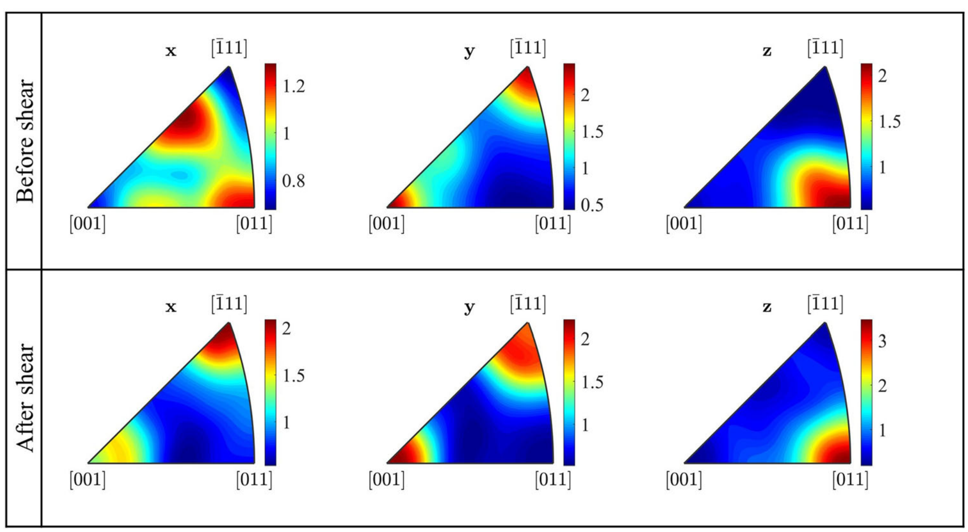

Conclusion

In summary, the dynamic mechanical behavior at high strain rates of 316L SS fabricated via DED additive manufacturing is examined. The microstructure evolution of adiabatic shear localization is characterized. AM 316L SS exhibits microstructure anisotropy and heterogeneity induced by grain morphologies and misorientation gradients. A step response giving rise to a plateau in the misorientation profiles correlates well with melt pool boundaries. Compared with conventional metals, AM metals have unique microstructural features, such as the typical melt pool boundary, gradational columnar-shaped grain morphology, and high as-built dislocation density. AM 316L SS demonstrates an enhanced mechanical strength compared with conventional wrought 316L SS under quasi-static compression. AM 316L SS exhibits nearly rate-insensitive responses in its yield stress, while strain-rate-induced strength enhancement is observed in conventional wrought 316L SS. In particular, after dynamic plastic deformation, the dislocation density of AM 316L SS barely increases. Based on a calculation of the difference in grain sizes, it is evident that the Hall–Petch effect only accounts for the partial increase in the yield strength. The high as-built GND density of AM 316L SS is the dominant strengthening factor. The dynamic shear elongation-to-failure of AM 316L SS is closely related to the complex grain morphology and high-density dislocation. Even if AM 316L SS has a high intrinsic strain hardening capability, the fracture strength ultimately limits the ductility. The grain size near the adiabatic shear localization region is noticed to be significantly refined. Thermal softening occurs in the localized region of plastic deformation, and the initial morphology of columnar grains growing along different melt pools formed via the additive manufacturing process almost changes completely.

To unlock the design potential of metallic AM with engineering applications, special attention to the dynamic responses is needed in three aspects including the rate insensitivity under dynamic loading, noteworthy reduction in ductility, and influences of high as-built dislocation densities and the process-dependent microstructure. In addition, post-processing with emphasis on the dynamic performance of AM metals and alloys needs to be further explored.

Acknowledgements

The authors gratefully acknowledge the funding support from the National Natural Science Foundation of China under Grants 11702089 and 11922206.

Funding

This study was funded by the National Natural Science Foundation of China (grant numbers 11702089 and 11922206).

Declarations

Conflict of Interest The authors declare that they have no conflict of interest.

Appendix A The distributions of GND density before and after dynamic shear loading

The histograms and normalized distributions of GND densities before and after dynamic loading are shown in Figure 14. The reduction in the number of data points after the dynamic test is due to lower quality in diffraction signals near highly deformed regions.

Appendix B Effect of shear deformation on orientation distribution

The orientation distribution functions obtained for the AM $S_{\parallel}$ and $S_{\perp}$ specimens before and after shear deformation are plotted in Figure 15.

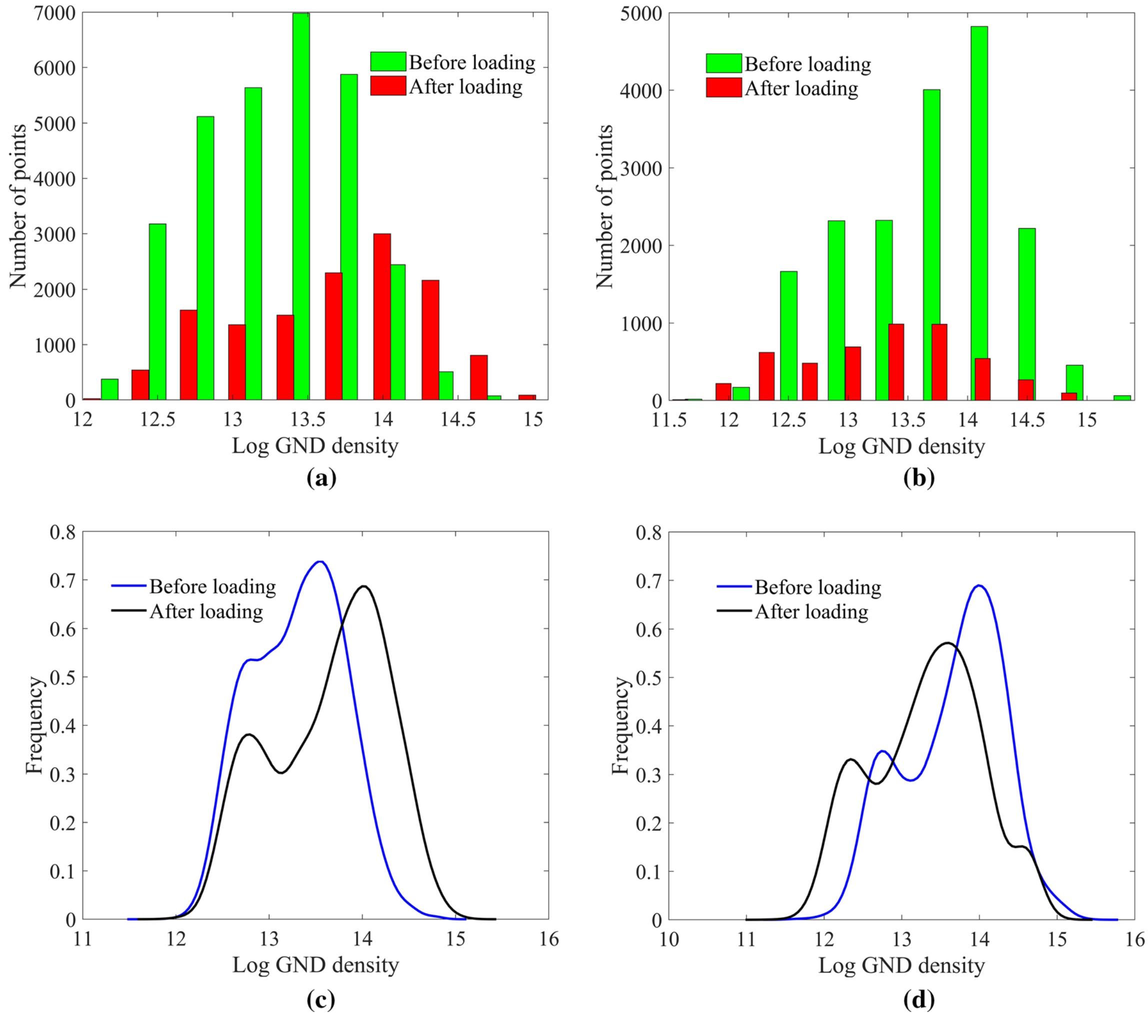

Figure 14 The histograms of GND densities of (**a**) the $S_{\parallel}$ specimen and (**b**) the $S_{\perp}$ specimen; the normalized distributions of GND densities of (**c**) the $S_{\parallel}$ specimen and (**d**) the $S_{\perp}$ specimen.

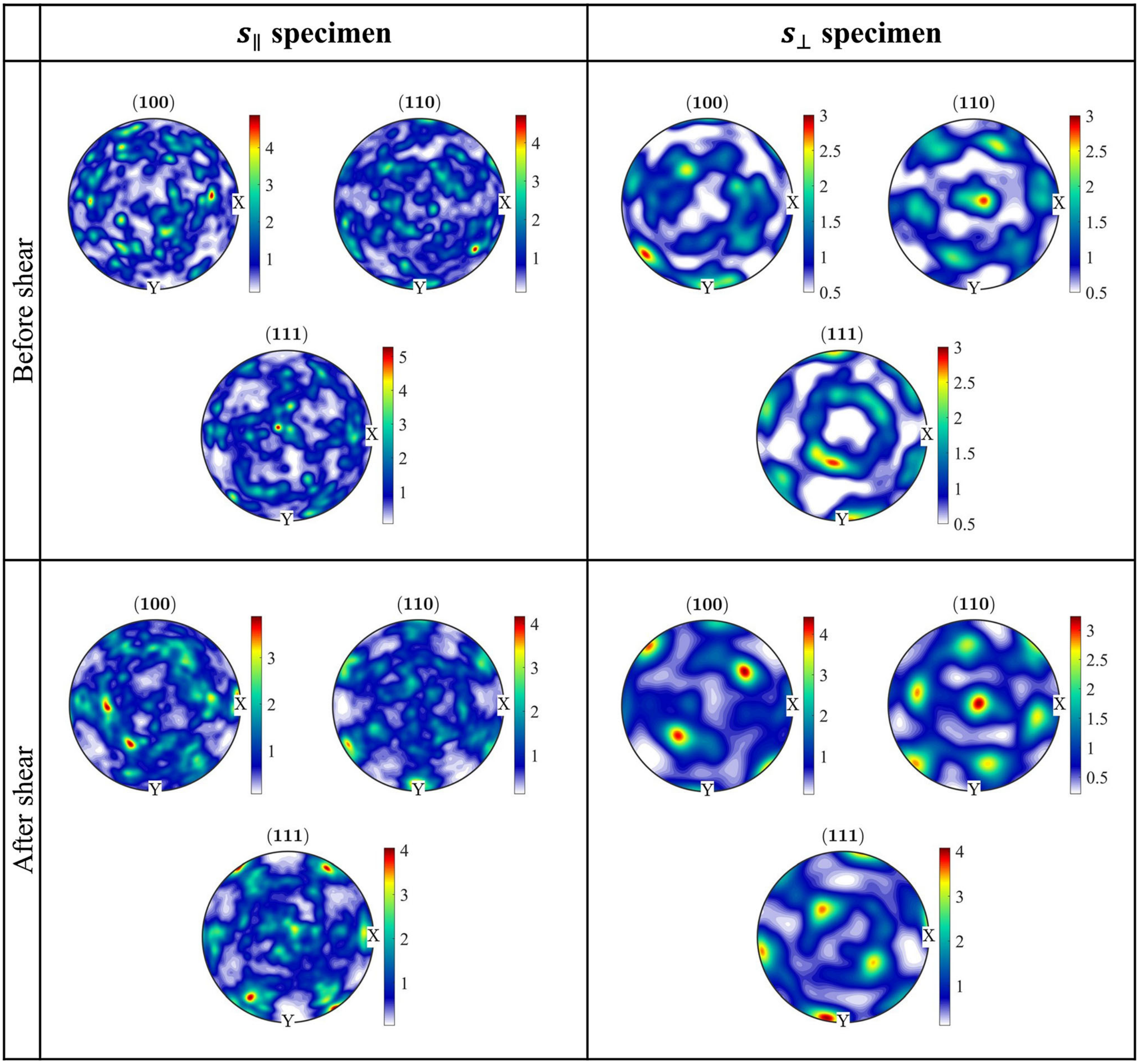

Figure 15 The (100, 110, 111) pole figure maps for the $S_{\|}$ and $S_{\perp}$ specimen before and after shear deformation.

References

[1] Haghdadi N, Laleh M, Moyle M, Primig S (2021) Additive manufacturing of steels: a review of achievements and challenges. J Mater Sci 56(1):64–107

[2] DebRoy T, Wei HL, Zuback JS, Mukherjee T, Elmer JW, Milewski JO, Beese AM, Wilson-Heid A, De A, Zhang W (2018) Additive manufacturing of metallic components - process, structure and properties. Prog Mater Sci 92:112–224

[3] Herzog D, Seyda V, Wycisk E, Emmelmann C (2016) Additive manufacturing of metals. Acta Mater 117:371–392

[4] Thompson MK, Moroni G, Vaneker T, Fadel G, Campbell RI, Gibson I, Bernard A, Schulz J, Graf P, Ahuja B, Martina F (2016) Design for additive manufacturing: trends, opportunities, considerations, and constraints. CIRP Ann 65(2):737–760

[5] Wu M-W, Lai P-H, Chen J-K (2016) Anisotropy in the impact toughness of selective laser melted Ti-6Al-4V alloy. Mater Sci Eng A 650:295–299

[6] Simson T, Emmel A, Dwars A, Bühm J (2017) Residual stress measurements on AISI 316L samples manufactured by selective laser melting. Addit Manuf 17:183–189
[7] Chauvet E, Kontis P, Jägle EA, Gault B, Raabe D, Tassin C, Blandin J-J, Dendievel R, Vayre B, Abed S, Martin G (2018) Hot cracking mechanism affecting a non-weldable Ni-based superalloy produced by selective electron beam melting. Acta Mater 142:82–94
[8] Yue H, Peng H, Li R, Qi K, Zhang L, Lin J, Su Y (2021) Effect of heat treatment on the microstructure and anisotropy of tensile properties of TiAl alloy produced via selective electron beam melting. Mater Sci Eng A 803:140473
[9] Ngo TD, Kashani A, Imbalzano G, Nguyen KTQ, Hui D (2018) Additive manufacturing (3d printing): A review of materials, methods, applications and challenges. Compos B Eng 143:172–196
[10] Smith TR, Sugar JD, San Marchi C, Schoenung JM (2019) Strengthening mechanisms in directed energy deposited austenitic stainless steel. Acta Mater 164:728–740
[11] Wang X, He X, Wang T, Li Y (2020) The influence of the microtexture and orientation of columnar grains on the fatigue crack growth of directed energy deposited Ti-6.5Al-2Zr-Mo-V alloys. Addit Manuf 35:101174
[12] Tofail SAM, Koumoulos EP, Bandyopadhyay A, Bose S, O'Donoghue L, Charitidis C (2018) Additive manufacturing: scientific and technological challenges, market uptake and opportunities. Mater Today 21(1):22–37
[13] Kok Y, Tan XP, Wang P, Nai MLS, Loh NH, Liu E, Tor SB (2018) Anisotropy and heterogeneity of microstructure and mechanical properties in metal additive manufacturing: A critical review. Mater Des 139:565–586
[14] Zheng B, Haley JC, Yang N, Yee J, Terrassa KW, Zhou Y, Lavernia EJ, Schoenung JM (2019) On the evolution of microstructure and defect control in 316L SS components fabricated via directed energy deposition. Mater Sci Eng A 764:138243
[15] Polonsky AT, Lenthe WC, Echlin MP, Livescu V, Gray GT, Pollock TM (2020) Solidification-driven orientation gradients in additively manufactured stainless steel. Acta Mater 183:249–260
[16] Melia MA, Carroll JD, Whetten SR, Esmaeely SN, Locke J, White E, Anderson I, Chandross M, Michael JR, Argibay N, Schindelholz EJ, Kustas AB (2019) Mechanical and corrosion properties of additively manufactured cocrfemnni high entropy alloy. Addit Manuf 29:100833
[17] Pham MS, Dovgyy B, Hooper PA (2017) Twinning induced plasticity in austenitic stainless steel 316L made by additive manufacturing. Mater Sci Eng A 704:102–111
[18] Suryawanshi J, Prashanth KG, Scudino S, Eckert J, Prakash O, Ramamurty U (2016) Simultaneous enhancements of strength and toughness in an Al-12Si alloy synthesized using selective laser melting. Acta Mater 115:285–294
[19] Wang Z, Palmer TA, Beese AM (2016) Effect of processing parameters on microstructure and tensile properties of austenitic stainless steel 304L made by directed energy deposition additive manufacturing. Acta Mater 110:226–235
[20] Gorsse S, Hutchinson C, Gouné M, Banerjee R (2017) Additive manufacturing of metals: a brief review of the characteristic microstructures and properties of steels, Ti-6Al-4V and high-entropy alloys. Sci Technol Adv Mater 18(3):584–610
[21] Arriaga M, Waisman H (2017) Combined stability analysis of phase-field dynamic fracture and shear band localization. Int J Plast 96:81–119
[22] Xu Z, He X, Han Y, Huang F (2020) A different viewpoint on mechanism of fracture to shear-banding failure mode transition. J Mech Phys Solids 145:104165
[23] Epperly EN, Sills RB (2020) Transient solute drag and strain aging of dislocations. Acta Mater 193:182–190
[24] Austin RA, McDowell DL (2011) A dislocation-based constitutive model for viscoplastic deformation of fcc metals at very high strain rates. Int J Plast 27(1):1–24
[25] Guo Y, Ruan Q, Zhu S, Wei Q, Lu J, Hu B, Wu X, Li Y (2020) Dynamic failure of titanium: Temperature rise and adiabatic shear band formation. J Mech Phys Solids 135:103811
[26] Li Z, Zhao S, Alotaibi SM, Liu Y, Wang B, Meyers MA (2018) Adiabatic shear localization in the CrMnFeCoNi high-entropy alloy. Acta Mater 151:424–431
[27] Roux E, Longère P, Cherrier O, Millot T, Capdeville D, Petit J (2015) Analysis of ASB assisted failure in a high strength steel under high loading rate. Mater Des 75:149–159
[28] Lee T, Nassiri A, Dittrich T, Vivek A, Daehn G (2020) Microstructure development in impact welding of a model system. Scripta Mater 178:203–206
[29] Gray GT, Livescu V, Rigg PA, Trujillo CP, Cady CM, Chen SR, Carpenter JS, Lienert TJ, Fensin SJ (2017) Structure/property (constitutive and spallation response) of additively manufactured 316L stainless steel. Acta Mater 138:140–149
[30] Laurençon M, de Rességuier T, Loison D, Baillargeat J, Ngnekou JND, Nadot Y (2019) Effects of additive manufacturing on the dynamic response of AlSi10Mg to laser shock loading. Mater Sci Eng A 748:407–417
[31] Alaghmandfard R, Dharmendra C, Odeshi AG, Mohammadi M (2020) Dynamic mechanical properties and failure characteristics of electron beam melted Ti-6Al-4V under high strain rate impact loadings. Mater Sci Eng A 793:139794
[32] Ran C, Chen P, Li L, Zhang W (2017) Dynamic shear deformation and failure of Ti-5Al-5Mo-5V-1Cr-1Fe titanium alloy. Mater Sci Eng A 694:41–47

[33] Fadida R, Rittel D, Shirizly A (2015) Dynamic mechanical behavior of additively manufactured Ti6Al4V with controlled voids. J Appl Mech 82(4):041004

[34] Pratheesh Kumar S, Elangovan S, Mohanraj R, Sathya Narayanan V (2021) Significance of continuous wave and pulsed wave laser in direct metal deposition. Mater Today: Proc 46:8086–8096

[35] Clos R, Schreppel U, Veit P (2003) Temperature, microstructure and mechanical response during shear-band formation in different metallic materials. In: Journal de Physique IV France, vol. 110, pp. 111–116

[36] Peirs J, Verleysen P, Degrieck J, Coghe F (2010) The use of hat-shaped specimens to study the high strain rate shear behaviour of Ti-6Al-4V. Int J Impact Eng 37(6):703–714

[37] Karthik GM, Kim HS (2021) Heterogeneous aspects of additive manufactured metallic parts: A review. Met Mater Int 27:1–39

[38] Sofinowski KA, Raman S, Wang X, Gaskey B, Seita M (2021) Layer-wise engineering of grain orientation (lego) in laser powder bed fusion of stainless steel 316L. Addit Manuf 38:101809

[39] Guglielmi PO, Ziehmer M, Lilleodden ET (2018) On a novel strain indicator based on uncorrelated misorientation angles for correlating dislocation density to local strength. Acta Mater 150:195–205

[40] Rezvanian O, Zikry M, Rajendran A (2007) Statistically stored, geometrically necessary and grain boundary dislocation densities: microstructural representation and modelling. Proc Royal Soc A: Math, Phys Eng Sci 463:2833–2853

[41] Schayes C, Bouquerel J, Vogt J-B, Palleschi F, Zaefferer S (2016) A comparison of EBSD based strain indicators for the study of Fe-3Si steel subjected to cyclic loading. Mater Charact 115:61–70

[42] Jariwala S, Sun H, Adhyaksa GWP, Lof A, Muscarella LA, Ehrler B, Garnett EC, Ginger DS (2019) Local Crystal Misorientation Influences Non-radiative Recombination in Halide Perovskites. Joule 3(12):3048–3060

[43] Carroll BE, Palmer TA, Beese AM (2015) Anisotropic tensile behavior of Ti-6Al-4V components fabricated with directed energy deposition additive manufacturing. Acta Mater 87:309–320

[44] Chen L, Liu W, Song L (2021) A multiscale investigation of deformation heterogeneity in additively manufactured 316L stainless steel. Mater Sci Eng A 820:141493

[45] Ma K, Wen H, Hu T, Topping TD, Isheim D, Seidman DN, Lavernia EJ, Schoenung JM (2014) Mechanical behavior and strengthening mechanisms in ultrafine grain precipitation-strengthened aluminum alloy. Acta Mater 62:141–155

[46] Busby JT, Hash MC, Was GS (2005) The relationship between hardness and yield stress in irradiated austenitic and ferritic steels. J Nucl Mater 336(2):267–278

[47] Smith TR, Sugar JD, Schoenung JM, San Marchi C (2018) Anomalous annealing response of directed energy deposited type 304L austenitic stainless steel. JOM 70(3):358–363

[48] Mishra A, Martin M, Thadhani NN, Kad BK, Kenik EA, Meyers MA (2008) High-strain-rate response of ultra-fine-grained copper. Acta Mater 56(12):2770–2783

[49] Waseda O, Veiga RG, Morthomas J, Chantrenne P, Becquart CS, Ribeiro F, Jelea A, Goldenstein H, Perez M (2017) Formation of carbon cottrell atmospheres and their effect on the stress field around an edge dislocation. Scripta Mater 129:16–19

[50] Chu D, Li X, Liu Z, Cheng J, Wang T, Li Z, Zhuang Z (2019) A unified phase field damage model for modeling the brittle-ductile dynamic failure mode transition in metals. Eng Fract Mech 212:197–209

[51] Lieou CKC, Bronkhorst CA (2018) Dynamic recrystallization in adiabatic shear banding: Effective-temperature model and comparison to experiments in ultrafine-grained titanium. Int J Plast 111:107–121

[52] Wright SI, Nowell MM, Field DP (2011) A review of strain analysis using electron backscatter diffraction. Microsc Microanal 17(3):316–329

[53] Gao B, Lai Q, Cao Y, Hu R, Xiao L, Pan Z, Liang N, Li Y, Gang S, Liu M, Zhou H, Wu X, Zhu Y (2020) Ultrastrong low-carbon nanosteel produced by heterostructure and interstitial mediated warm rolling. Sci Adv 6:8169–8192

[54] Luo ZC, Huang MX (2018) Revisit the role of deformation twins on the work-hardening behaviour of twinning-induced plasticity steels. Scripta Mater 142:28–31

[55] Wu X, Yang M, Yuan F, Wu G, Wei Y, Huang X, Zhu Y (2015) Heterogeneous lamella structure unites ultrafine-grain strength with coarse-grain ductility. Proc Natl Acad Sci 112(47):14501–14505

[56] Zepeda-Ruiz LA, Stukowski A, Oppelstrup T, Bertin N, Barton NR, Freitas R, Bulatov VV (2021) Atomistic insights into metal hardening. Nat Mater 20:315–325

[57] Lins JFC, Sandim HRZ, Kestenbach H-J, Raabe D, Vecchio KS (2007) A microstructural investigation of adiabatic shear bands in an interstitial free steel. Mater Sci Eng A 457(1):205–218

Publisher's Note Springer Nature remains neutral with regard to jurisdictional claims in published maps and institutional affiliations.